



ELSEVIER

Journal of Nuclear Materials 244 (1997) 266–272

**Journal of  
nuclear  
materials**

# In situ observation of defect growth beyond the irradiated region in yttria-stabilized zirconia induced by 400 keV xenon ion-beam at $-90$ and $30^{\circ}\text{C}$ <sup>1</sup>

Ning Yu<sup>\*</sup>, Kurt E. Sickafus, Padma Kodali, Michael Nastasi*Materials Science and Technology Division, Los Alamos National Laboratory, Los Alamos, New Mexico 87545, USA*

Received 5 February 1996; accepted 13 May 1996

## Abstract

Single crystals of yttria-stabilized zirconia (YSZ) were irradiated with 400 keV Xe ion-beam at room temperature and  $-90^{\circ}\text{C}$ . Defect growth was monitored in situ with Rutherford Backscattering and ion channeling (RBS/C) techniques using a 2 MeV He ion-beam. The irradiated YSZ was observed to consist of a 60 nm less-damaged or defect-denuded top layer, followed by a highly disordered layer. Ion channeling revealed that the degree of lattice disorder saturated at 70% of the random level in the bottom layer. At a dose of  $3 \times 10^{20}$  Xe/m<sup>2</sup>, this layer extended to a depth of 160 nm, well beyond the irradiated depth ( $< 110$  nm). Cross-sectional transmission electron microscopy observations along with RBS measurements are interpreted as indicating the presence of small Xe precipitates with an average diameter of 3 nm, uniformly distributed over the 20–110 nm depth. The study demonstrated that point defects generated in the Xe-irradiated region diffused and produced stable extended structural defects at depths beyond the irradiated region.

## 1. Introduction

Many studies have focused on searching for radiation resistant ceramics and on understanding their radiation responses (for a review, see Refs. [1,2]). Magnesium aluminate spinel (MgAl<sub>2</sub>O<sub>4</sub>) has been demonstrated to be one of the most radiation resistant oxides under fast neutron irradiation [3–6] and ion irradiation [7] at elevated temperature up to 10–250 displacements per atom (dpa). However, it has been observed that spinel undergoes phase transformations from its equilibrium phase through an intermediate crystalline phase to an amorphous phase under ion irradiation at cryogenic temperatures [8,9]. This indicates that point-defect mobility that varies with irradiation temperature plays an important role during microstruc-

tural evolution in spinel. Therefore, we have extended our study on temperature dependence of radiation effects to other relevant oxides, including alpha-alumina ( $\alpha\text{-Al}_2\text{O}_3$ ) [10], geikielite (MgTiO<sub>3</sub>) [10], ilmenite (FeTiO<sub>3</sub>) [10], magnesia (MgO), rutile (TiO<sub>2</sub>), and yttria-stabilized zirconia (YSZ). All these studies have taken advantage of the in situ ion beam facility at Los Alamos National Laboratory (LANL) [11,12].

Previous studies [13,14] have shown that YSZ cannot be amorphized by Xe ion irradiation at room temperature. Transmission electron microscopy (TEM) studies revealed that high doses of Xe irradiation,  $3\text{--}10 \times 10^{20}$  Xe/m<sup>2</sup>, into a TEM thin foil of YSZ resulted in formation of solid or fluid Xe embedded in the film. In this study, we have examined in situ the kinetics of radiation damage accumulation in YSZ induced by 400 keV Xe ion irradiation at temperatures of 30 and  $-90^{\circ}\text{C}$ . The radiation damage behavior was found to be the same at these two temperatures. The irradiated YSZ was observed to consist of a less damaged or defect-denuded top layer of 60 nm thickness, followed by a highly disordered layer. The lattice disorder reached a saturation level in the bottom layer while its

<sup>\*</sup> Corresponding author. Permanent address: Semiconductor Process and Device Center, Texas Instruments, Inc., MS 944, P.O. Box 655012, Dallas, TX 75265, USA. Tel.: +1-972 927 3488; fax: +1-972 995 1916; e-mail: nyu@spdc.ti.com.

<sup>1</sup> Presented at the TMS'96 Meeting.

thickness increased towards a depth (160 nm) deeper than the irradiated depth (< 110 nm). The study demonstrated that point defects generated in the Xe-irradiated region diffused and produced large extended defects at the depth beyond the irradiated region.

## 2. Experiment

YSZ single crystals ( $\text{ZrO}_2$ ), containing 9.4 mol%  $\text{Y}_2\text{O}_3$  and in a dimension of  $10 \times 10 \text{ mm}^2$  width and 0.5 mm thickness, were used in this study. The samples, oriented along the (001) axis and polished to an optical finish, were coated with a 20 nm carbon film to avoid surface charging during ion irradiation and ion-beam analysis. The ion irradiation experiments were performed at the LANL in situ ion beam facility [11,12]. The LANL facility consists of a 200 kV ion implanter beamline and a 3 MV tandem ion beamline. These were used for ion irradiation and ion-beam analysis, respectively, i.e., Rutherford backscattering and ion channeling (RBS/C) measurement, on a bulk single crystal sample, as shown in Fig. 1. An YSZ sample for the in situ experiment was mounted onto a sample stage with silver paint. The orientation and translational motions of the sample were controlled by a multi-axis goniometer. Prior to ion irradiation, the 2 MeV  $\text{He}^+$  ion-beam from the tandem accelerator was aligned along the (011) axis of the unirradiated YSZ sample using RBS/C measurements. This orientation was kept throughout the entire in situ experiment to ensure the same channeling measurement conditions.

Radiation damage was introduced by a 400 keV  $\text{Xe}^{2+}$

ion-beam incident at a  $15^\circ$  angle to the sample normal at temperatures of 30 and  $-90^\circ\text{C}$ . Radiation-induced lattice disorder was monitored through a sequential RBS/C measurement up to a charge of  $4 \mu\text{C}$  following each incremental dose of Xe irradiation. The irradiation and analysis beam spots were co-centered on the sample surface with beam sizes of about 7 and 2 mm in diameter, respectively. The irradiation doses varied from  $2 \times 10^{17}$  to  $3 \times 10^{20} \text{ Xe/m}^2$  with the irradiation beam flux maintained at  $\sim 1 \times 10^{17} \text{ Xe/m}^2\text{s}$ . The irradiation experiment at room temperature was first performed and proceeded until the lattice disorder in the irradiated YSZ reached a certain saturation level. Then the sample was translated to set an unirradiated area and cooled to  $-90^\circ\text{C}$  for a second irradiation experiment. After irradiation to the highest doses, random RBS spectra were taken while the sample was rocking off the channeling directions.

The projected range and the damage peak of 400 keV Xe ions at a  $15^\circ$  incident angle were estimated to be 75 and 50 nm, respectively, by the TRIM code [15] using a mass density of  $5.6 \text{ g/cm}^3$  for YSZ. The damage level in the peak damage region was estimated to be 27 dpa for a dose of  $1 \times 10^{20} \text{ Xe/m}^2$  assuming a displacement energy of 40 eV for all elements. The peak concentration of implanted Xe was about 2 at% for  $1 \times 10^{20} \text{ Xe/m}^2$  in YSZ.

Following the in situ experiments, the irradiated YSZ samples were further examined with RBS/C at room temperature. The samples were then prepared into electron transparent specimens for cross-sectional transmission electron microscopy (XTEM) examination. The radiation-induced microstructures were examined in a Philips CM 30 microscope operated at 300 kV using bright-field and dark-field XTEM techniques.

The LANL facility plays a complementary role to the high-voltage electron microscopy and tandem (HVEM-tandem) facility at Argonne National Laboratory (ANL). Fig. 1 shows a comparison of the LANL in situ experiment with the ANL in situ experiment. The ANL facility combines a 2 MV tandem ion beamline with an 1 MV electron microscope to perform ion irradiation and electron diffraction on an electron-transparent TEM thin foil, 50 nm thick and mounted on a TEM grid. The LANL experiment effectively determines the depth profile of radiation damage and the evolution of lattice disorder, while the ANL experiment directly monitors the radiation-induced phase transformations. In the ANL experiment, the TEM thin foil may limit the irradiation beam current in order to avoid beam heating effects. In addition, point defect annihilation at the specimen surfaces can delay phase transformations. In the LANL experiment, the larger volume of a bulk sample allows a higher irradiation-beam current and causes less surface effects. For a large bulk sample, a set of irradiation experiments can be conducted in series at different temperatures by translating the sample without breaking the vacuum (Fig. 1).

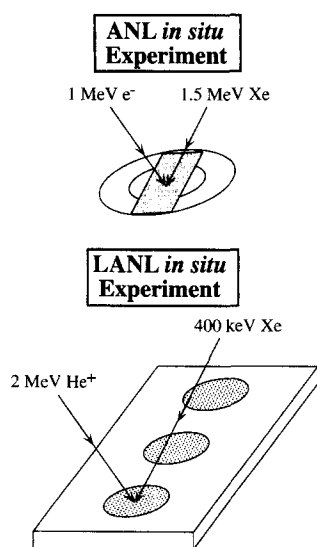


Fig. 1. Schematic drawings of in situ characterization of ion-irradiation induced phenomena using transmission electron microscopy and ion-beam analysis.

The LANL in situ capability shortens the experimental cycle typically by one order of magnitude and improves the experimental reliability as compared to conventional ex situ experiments. The conditions of the sample surface, the ion irradiation, the channeling alignment, and the characterization contribute to the uncertainty of the ex situ experiments. However, these variations are significantly minimized in the in situ experiments. Furthermore, during an in situ experiment, we can dynamically monitor the changes in the damage profile and control the incremental irradiation dose correspondingly. Therefore, radiation-induced phenomena can be carefully evaluated and resolved, and the corresponding microstructures can be determined by further ex situ TEM examination. The in situ experiment also maintains the same experimental environment for both irradiation and characterization of the sample. This eliminates the possibility of altering the sample conditions for the characterization purposes. Experimental results are thus more reliable for in situ measurements as compared to ex situ measurements.

### 3. Results

Fig. 2 shows some representatives of 18 sequential in situ (011) RBS/C spectra from the YSZ crystal following the 400 keV Xe irradiations at room temperature. The spectra are plotted as normalized yield obtained by normalizing the backscattering counts with the collected He charge and the detector solid angle. Minimum backscattering yield, defined as the RBS yield ratio of an aligned spectrum to a random spectrum, is a measure of the degree of crystal quality or lattice disorder. A minimum yield of 10% for

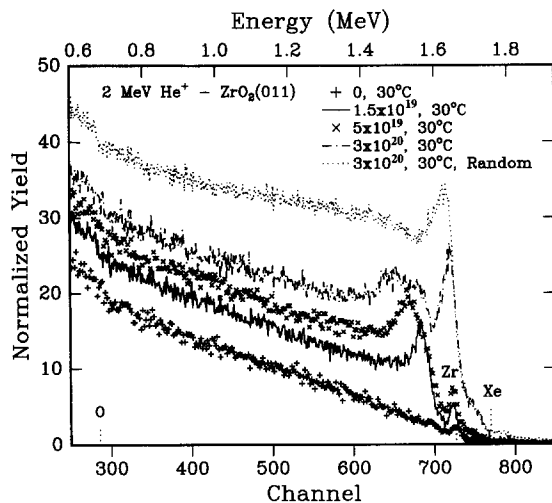


Fig. 2. In situ RBS/C spectra obtained from an YSZ crystal using a 2 MeV He ion-beam incident along the (011) axis following sequential 400 keV Xe irradiations at 30°C, along with a random spectrum from the YSZ crystal irradiated to the highest dose.

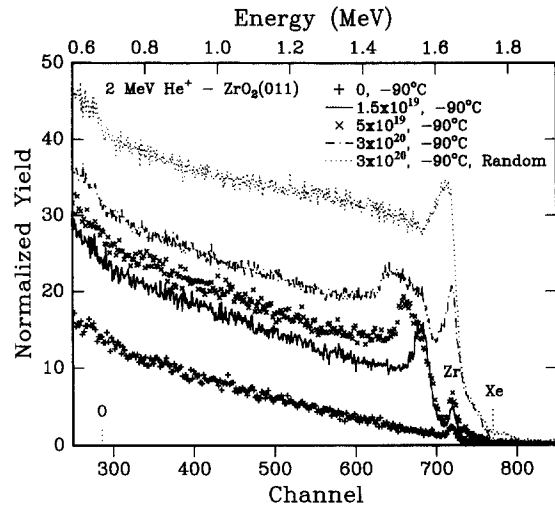


Fig. 3. In situ RBS/C spectra obtained from an YSZ crystal using a 2 MeV He ion-beam incident along the (011) axis following sequential 400 keV Xe irradiations at  $-90^{\circ}\text{C}$ , along with a random spectrum from the YSZ crystal irradiated to the highest dose.

the Zr signal near the sample surface indicates good single crystallinity of the unirradiated sample. Following an irradiation dose of  $1.5 \times 10^{19}$  Xe/m<sup>2</sup>, a damaged layer appears around the damage peak at the depth of 60 nm, as indicated by the higher dechanneling yield around the Channel Number of 680 in the channeling spectrum. However, the 60 nm top layer remains less damaged or defect-denuded. After irradiation to a dose of  $5 \times 10^{19}$  Xe/m<sup>2</sup>, no significant increase in the dechanneling is observed within the top layer. However, it is intriguing to note that the damaged layer grows deeper. The sharp interface between the bottom damaged zone and the top denuded zone is retained. At this stage, the damage-growing front at the 120 nm depth is definitely beyond the entire Xe-irradiated layer ( $< 110$  nm) where lattice atoms experienced displacements. As the irradiation dose increases to  $1.5\text{--}3 \times 10^{20}$  Xe/m<sup>2</sup>, a significant increase in the channeling yield in the top layer is observed. However, this increase is in part due to the overlap of the implanted Xe signal with the Zr signal. Excluding the contribution of the Xe signal, the minimum yield in the top layer appeared to be less than 50%. The sharp interface between the surface denuded zone and the underlying damaged zone is maintained. The damaged zone is extended to a depth of 160 nm at a dose  $3 \times 10^{20}$  Xe/m<sup>2</sup> with the minimum yield saturated at 70% of the random level. This indicates saturation of lattice disorder in the bottom zone.

Similar behavior of radiation damage is observed in YSZ irradiated with Xe ions at  $-90^{\circ}\text{C}$ , as shown by in situ RBS/C spectra taken at the same temperature in Fig. 3. The minimum yield appears to be 7% for the Zr in the unirradiated YSZ. The lower minimum yield value, as

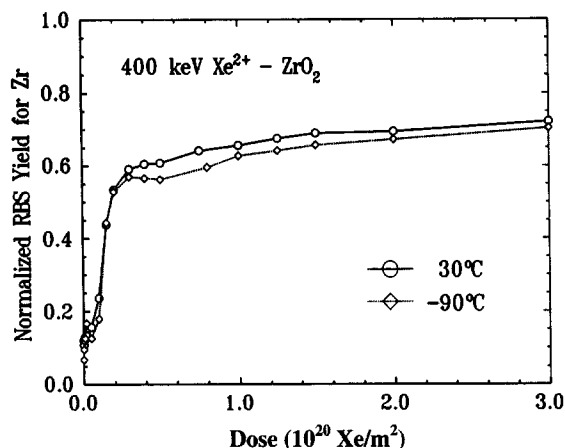


Fig. 4. The minimum yield of Zr from the highly disordered zone in YSZ versus Xe irradiation dose at the irradiation temperatures of 30 and  $-90^{\circ}\text{C}$ .

compared to that obtained at room temperature (10% in Fig. 2), is due to the reduction in lattice vibration at a lower temperature. A defect-denuded top layer is retained in the YSZ irradiated to doses of  $1.5\text{--}5 \times 10^{19} \text{Xe}/\text{m}^2$ , followed by a heavily damaged layer starting at a 60 nm depth. Following sequential irradiations, the interface between the top and bottom layer remains unchanged while the bottom layer grows to a depth of 160 nm. The minimum yield of the bottom layer saturates at 70% of the random level at a dose of  $3 \times 10^{20} \text{Xe}/\text{m}^2$ . A big hump that appears at the shoulder of the surface Zr in the random spectrum, taken from the  $3 \times 10^{20} \text{Xe}/\text{m}^2$  irradiated YSZ, is caused by the implanted Xe signal.

The kinetics of radiation damage accumulation in YSZ are determined from the sequence of in situ RBS/C spectra following the Xe irradiations. Fig. 4 shows the values of minimum yield from the heavily damaged zone for the Zr sublattice as a function of irradiation dose and temperature. The kinetic curve of room temperature shows a rapid rise in the minimum yield from 10% to 60% as the irradiation dose increases from 0 to  $2.5 \times 10^{19} \text{Xe}/\text{m}^2$ . The degree of lattice disorder in this zone then levels off at a dose of  $2.5 \times 10^{19} \text{Xe}/\text{m}^2$  and the minimum yield only increases slightly from 60% to 70% as the dose increases to  $3 \times 10^{20} \text{Xe}/\text{m}^2$ . This indicates that the lattice disorder saturates for a dose of  $2.5 \times 10^{19} \text{Xe}/\text{m}^2$ . The kinetic curve of  $-90^{\circ}\text{C}$  behaves similarly as that of  $30^{\circ}\text{C}$ . Overall, there is a reduction of about 0.03 in the minimum yield for the  $-90^{\circ}\text{C}$  curve as compared to that of  $30^{\circ}\text{C}$ . This can be solely attributed to the temperature dependence of the lattice vibration. In a defective crystal, both the lattice disorder and the lattice vibration add to the minimum yield. A decrease in the temperature results in a decrease in the lattice vibration that reduces the minimum yield. Taking the lattice vibration into account, the room temperature curve falls onto the low temperature curve. The

results in Fig. 4 indicate that the damage accumulation induced by Xe irradiation is independent of the irradiation temperature, at least in the range from  $-90$  to  $30^{\circ}\text{C}$ .

The independence of damage accumulation on the irradiation temperature is further confirmed by ex situ RBS/C measurement. Fig. 5 shows (001) RBS/C spectra acquired at room temperature from the YSZ crystals irradiated to  $3 \times 10^{20} \text{Xe}/\text{m}^2$  at 30 and  $-90^{\circ}\text{C}$ , respectively. The profiles of lattice disorder for the Zr are identical following the Xe irradiations at two different temperatures. A small step near the edge of the surface Zr represents the implanted Xe. Simulation (Ref. [16], using the RUMP code) of the random spectrum from the  $3 \times 10^{20} \text{Xe}/\text{m}^2$  irradiated YSZ reveals a relatively uniform distribution of 4 at% Xe over the depth 20–110 nm. The heavily damaged zone is found to distribute at the depths of 60–160 nm. The TRIM code [15] predicts a near Gaussian distribution for the implanted Xe in YSZ. The uniform distribution of Xe determined by RBS indicates that the implanted Xe is significantly redistributed during the high dose of Xe irradiation. Furthermore, the heavily damaged zone is extended beyond the Xe-distributed zone. These observations indicate that the implanted Xe and the point defects are highly mobile in YSZ and their mobilities also appear to be independent of irradiation temperature from  $-90$  to  $30^{\circ}\text{C}$ .

The radiation-induced microstructures were examined on a YSZ sample irradiated to  $3 \times 10^{20} \text{Xe}/\text{m}^2$  at  $-90^{\circ}\text{C}$  using bright-field and dark-field XTEM techniques. Fig. 6(a) is a dark-field XTEM image taken with a  $[111]$  diffraction vector. Three microstructural zones are distinct in the image along the Xe-irradiation direction (vertical on

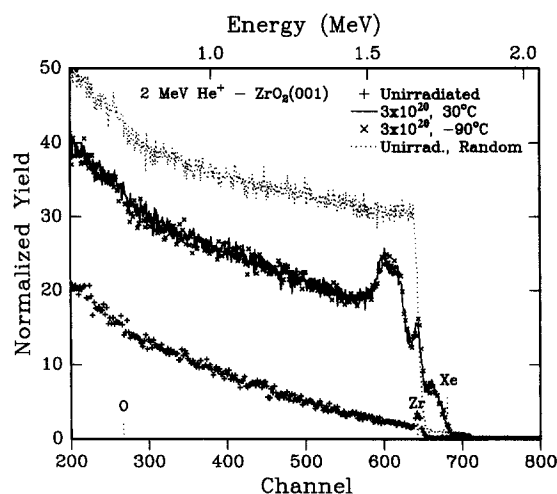


Fig. 5. Ex situ RBS/C spectra obtained from the YSZ crystals using a 2 MeV He ion-beam incident along the (001) axis before and after the Xe irradiations of 400 keV and  $3 \times 10^{20} \text{Xe}/\text{m}^2$  at 30 and  $-90^{\circ}\text{C}$ , respectively, along with a random spectrum from the unirradiated sample.

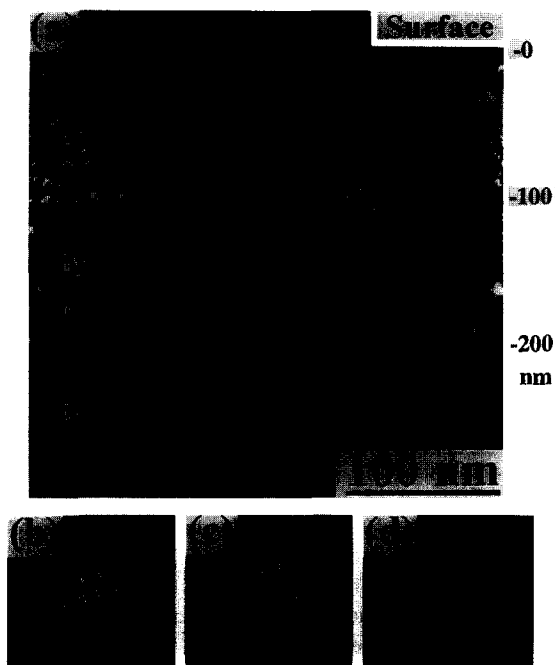


Fig. 6. (a) Dark-field XTEM image showing a Xe-rich layer (labeled '1') and a highly defected layer ('2'), followed by the unirradiated YSZ substrate ('3'), with  $g = [\bar{1}\bar{1}1]$ , along with (b), (c), and (d) microdiffraction patterns taken from the zones '1', '2', and '3', respectively.

the page). The bottom zone '3' represents the unirradiated and undamaged substrate region. The top zone, labeled '1', of 80 nm thickness shows a uniform distribution of small clusters with an average diameter of 3 nm. The second zone, labeled '2', of 100 nm thickness exhibits much larger extended defects with sizes of 5–20 nm. On the top portion of zone '2', about 40 nm thick, a mixture of small clusters and large structural defects are visible. The thickness of the zone '1' is close to that of the defect-denuded zone determined by RBS measurement (Figs. 3 and 5). No large structural defects are visible in this zone, in support of the RBS/C observation of the defect-denuded zone. The cluster features are similar to those observed in the  $2 \times 10^{21}$  Xe/m<sup>2</sup> implanted MgO [17], which were identified as solid or fluid Xe precipitates. The cluster diameters in Fig. 6(a), however, appear to be much smaller than those in the MgO (10–50 nm) probably due to the large difference in the Xe dose between these two cases. These smaller clusters can be interpreted as precipitates of solid Xe because fluid Xe forms in much larger sizes (> 10 nm) [13]. The zone '2' containing larger extended defects represents the heavily disordered zone, as observed by the channeling measurement in Fig. 5. The nature of the extended defects is under further investigation. A transition layer between the zones '1' and '2' indicates that part of the Xe precipitated zone overlaps with the highly disor-

dered zone. Inset microdiffraction patterns in Fig. 6(b), (c), and (d) were taken with short exposure times from the zones '1', '2', and '3', using a convergent electron-beam of 50 nm in diameter. No extra diffraction spots were observed from the zone '1'. Due to the short exposure times and the small sampling area, the additional reflections from solid Xe may not be detectable [13]. These diffraction patterns are identical and indicate that no phase transformation occurs in the Xe-irradiated zone and the highly defected zone.

#### 4. Discussion

By combining the RBS results with the XTEM results, schematic drawings are plotted in Fig. 7, showing the evolution of the distributions for implanted Xe ions and structural defects following Xe irradiation. In the early stage of Xe irradiation, the implanted Xe has a near Gaussian distribution centered at a depth of 75 nm, while the damage profile peaks at a shallower depth, 50 nm. A high dose of Xe irradiation results in significant accumulation of Xe and production of radiation damage in the irradiated layer to a depth of 110 nm below the surface. The implanted Xe and the point defects produced by cascade collisions appear to be mobile. A highly disordered zone initially develops near the damage peak and then gradually grows deeper. The lattice disorder reaches a saturation level in the heavily damaged zone and more point defects diffuse through this layer to make it grow thicker. In contrast, the top layer of 60 nm thickness remains relatively defect-denuded up to high doses. Accompanying the growth of the disordered zone, inward and outward diffusion of implanted Xe results in a uniform distribution of Xe precipitates over the depth of 20–110 nm.

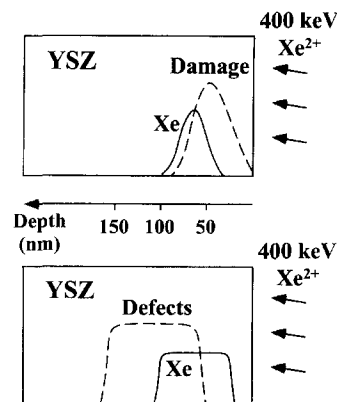


Fig. 7. Schematic drawing showing evolution of accumulation of implanted Xe ions and structural defects in the Xe-irradiated YSZ from a low dose (top) to a high dose (bottom).

The study clearly demonstrates the layer-by-layer growth of lattice disorder towards the deeper region beyond the irradiated region. It indicates that point defects generated in the irradiated region can diffuse through the highly disordered layer to grow new defects even at  $-90^{\circ}\text{C}$ . This presents the evidence of radiation-enhanced diffusion in YSZ. A high concentration of nonequilibrium point defects can readily annihilate within the irradiated region or diffuse out of the irradiated region and annihilate at sinks or form stable extended defect structures. Only the inward flux of point defects is expected to contribute to the growth of defect structures beyond the irradiated region. Two obvious factors can cause the inward flux, (a) concentration gradient of the generated point defects and (b) strain field induced by implanted Xe and stabilized defects. Fracture toughness of Xe-irradiated samples, measured by indentation techniques, have revealed a two-fold increase as compared to unirradiated samples. The higher fracture toughness confirms the presence of compressive stress in the Xe-irradiated layer. The compressive stress is consistent with a high concentration of Xe as well as some structural defects within the irradiated layer. The compressive stress may provide a significant driving force for inward diffusion of point defects.

Another important observation from Figs. 2–5 is that radiation damage accumulation in YSZ behaves the same at two different temperatures. Point-defect mobility appears not to change over the temperature range from  $-90$  to  $30^{\circ}\text{C}$ . Furthermore, no amorphization is observed in the YSZ irradiated with 400 keV Xe ions up to  $3 \times 10^{20}$  Xe/m<sup>2</sup> at  $-90^{\circ}\text{C}$  with a peak damage level equivalent to 110 dpa. The maximum lattice disorder saturates at the same level following irradiation at two different temperatures, as indicated by the 70% minimum yield. The defect saturation is consistent with that for 240 keV Xe irradiation at room temperature [13]. A recent study has also shown that no amorphization occurs in YSZ following the 400 keV Xe irradiation to  $3 \times 10^{20}$  Xe/m<sup>2</sup> even at  $-170^{\circ}\text{C}$  [18]. These observations suggest that point defects produced by ion irradiation are highly mobile in YSZ at cryogenic temperatures. The behavior observed in this study is in strong contrast to that of MgAl<sub>2</sub>O<sub>4</sub> [8] and  $\alpha$ -Al<sub>2</sub>O<sub>3</sub> [19], which showed increased lattice disorder with decreasing irradiation temperature due to the reduced mobility of point defects. Therefore, it is expected that an amorphous state would not be readily produced by radiation damage in the materials that do not exhibit enhanced radiation damage with decreasing temperature.

A defect-denuded zone of 60 nm thickness is clearly present in the Xe-irradiated YSZ, in particular up to a dose of  $5 \times 10^{19}$  Xe/m<sup>2</sup> in Figs. 2 and 3. After the  $3 \times 10^{20}$  Xe/m<sup>2</sup> irradiation, the higher minimum yield ( $\sim 40\%$ ) in this zone (Fig. 5) is mostly due to the presence of a high concentration of small Xe precipitates. As determined, the 4 at% Xe precipitates are distributed uniformly over the depth of 20–110 nm. The XTEM results in Fig. 6(a) show

no sign of other larger structural defects within this zone besides the small Xe precipitates. This supports that the precipitates and the resulting strain field may be the major cause for dechanneling in the defect-denuded zone. The denuded zone in YSZ irradiated at  $-90^{\circ}\text{C}$  is similar to that found in MgAl<sub>2</sub>O<sub>4</sub> spinel following ion irradiation at room temperature [7] or  $400^{\circ}\text{C}$  [20]. Zinkle has attributed the defect-denuded zone to the effective annihilation of point defects at the surface [7] and to ionization-enhanced diffusion [2].

## 5. Conclusions

We have studied in situ the kinetics of radiation damage accumulation in YSZ under 400 keV Xe ion irradiation at temperatures of 30 and  $-90^{\circ}\text{C}$ . The radiation damage behavior was found to be identical at these two temperatures and no amorphization was observed up to  $3 \times 10^{20}$  Xe/m<sup>2</sup> equal to 110 dpa for peak damage. The irradiated YSZ consisted of a defect-denuded top layer of 60 nm thickness, followed by a highly disordered layer. The lattice disorder reached a saturation level in the bottom layer while its thickness increased towards a great depth (160 nm), deeper than the irradiated depth ( $< 110$  nm). XTEM and RBS measurements are interpreted as indicating the presence of small Xe precipitates with an average diameter of 3 nm, uniformly distributed over the 20–110 nm depth. The study demonstrated that radiation-induced point defects are highly mobile and lead to the growth of stable defects at the depth beyond the irradiated region.

## Acknowledgements

We are grateful to Caleb Evans, Mark Hollander, and Joseph Tesmer for technical assistance with Xe ion irradiations. All ion beam work was performed at the Los Alamos Ion Beam Materials Laboratory. This research was sponsored by the U.S. Department of Energy, Office of Basic Energy Sciences, Division of Materials Sciences.

## References

- [1] L.W. Hobbs, F.W. Clinard, Jr., S.J. Zinkle and R.C. Ewing, *J. Nucl. Mater.* 216 (1994) 291.
- [2] S.J. Zinkle, *Nucl. Instrum. Methods B* 91 (1994) 234.
- [3] F.W. Clinard, Jr., G.F. Hurley and L.W. Hobbs, *J. Nucl. Mater.* 108–109 (1982) 655.
- [4] F.A. Garner, G.W. Hollenberg, F.D. Hobbs, J.L. Ryan, Z. Li, C.A. Black and R.C. Bradt, *J. Nucl. Mater.* 212–215 (1994) 1087.
- [5] K.E. Sickafus, A.C. Larson, N. Yu, M. Nastasi, G.W. Hollenberg, F.A. Garner and R.C. Bradt, *J. Nucl. Mater.* 219 (1995) 128.

- [6] C. Kinoshita, K. Fukumoto, K. Fukuda, F.A. Garner and G.W. Hollenberg, *J. Nucl. Mater.* 219 (1995) 143.
- [7] S.J. Zinkle, *J. Am. Ceram. Soc.* 72 (1989) 1343.
- [8] N. Yu, K.E. Sickafus and M. Nastasi, *Philos. Mag. Lett.* 70 (1994) 235; N. Yu, M. Nastasi, M.G. Hollander, C.R. Evans, C.J. Maggiore, K.E. Sickafus and J.R. Tesmer, *Mater. Res. Soc. Symp. Proc.* 316 (1994) 69.
- [9] N. Bordes, L.M. Wang, R.C. Ewing and K.E. Sickafus, *J. Mater. Res.* 10 (1995) 981.
- [10] J.N. Mitchell, N. Yu, K.E. Sickafus, M. Nastasi, T.N. Taylor, K.J. McClellan and G.L. Nord, *Res. Soc. Symp. Proc.* 396 (1996) 173.
- [11] N. Yu, M. Nastasi, T.E. Levine, J.R. Tesmer, M.G. Hollander, C.R. Evans and C.J. Maggiore, *Nucl. Instrum. Methods B* 99 (1995) 566.
- [12] N. Yu, T.E. Levine, K.E. Sickafus, M. Nastasi, J.N. Mitchell, C.J. Maggiore, C.R. Evans, M.G. Hollander, J.R. Tesmer, W.J. Weber and J.W. Mayer, *Nucl. Instrum. Methods B* 118 (1995) 766.
- [13] E.L. Fleischer, M.G. Norton, M.A. Zaleski, W. Hertl, C.B. Carter and J.W. Mayer, *J. Mater. Res.* 6 (1991) 1905.
- [14] E.L. Fleischer, W. Hertl, T.L. Alford, P. Borgesen and J.W. Mayer, *J. Mater. Res.* 5 (1990) 385.
- [15] J.F. Ziegler, J.P. Biersack and U. Littmark, *The Stopping and Range of Ions in Solids* (Pergamon, New York, 1985).
- [16] L.R. Doolittle, *Nucl. Instrum. Methods B* 9 (1985) 344.
- [17] M.G. Norton, E.L. Fleischer, W. Hertl, C.B. Carter, J.W. Mayer and E. Johnson, *Phys. Rev. B* 43 (1991) 9291.
- [18] N. Bordes, R.C. Ewing, K.E. Sickafus and M. Nastasi, (1996), to be published.
- [19] C.J. McHargue, G.C. Farlow, C.W. White, J.M. Williams, B.R. Appleton and H. Naramoto, *Mater. Sci. Eng.* 69 (1985) 123.
- [20] N. Yu, K.E. Sickafus and M. Nastasi, *Mater. Res. Soc. Symp. Proc.* 373 (1995) 401.